



Full Length Article

Microstructure and battery performance of Mg-Zn-Sn alloys as anodes for magnesium-air battery

Fanglei Tong^a, Xize Chen^a, Shanghai Wei^{a,*}, Jenny Malmström^{a,b}, Joseph Vella^c, Wei Gao^a

^aDepartment of Chemical & Materials Engineering, Faculty of Engineering, The University of Auckland, New Zealand

^bMacDiarmid Institute for Advanced Materials and Nanotechnology, Wellington, New Zealand

^cSchool of Chemical Science, Faculty of Science, The University of Auckland, New Zealand

Received 25 April 2021; received in revised form 1 August 2021; accepted 20 August 2021

Available online xxx

Abstract

Four Mg-xZn-ySn ($x = 2, 4$ and $y = 1, 3$ wt.%) alloys are investigated as anode materials for magnesium-air (Mg-air) battery. The self-corrosion and battery discharge behavior of these four Mg-Zn-Sn alloys are analyzed by electrochemical measurements and Mg-air battery tests. The results show that addition of Sn stimulates the electrochemical activity and significantly improves the anodic efficiency and specific capacity of Mg-Zn alloy anodes. Among the four alloy anodes, Mg-2Zn-3Sn (ZT23) shows the best battery discharge performance at low current densities (≤ 5 mA cm⁻²), achieving high energy density of 1367 mWh g⁻¹ at 2 mA cm⁻². After battery discharging, the surface morphology and electrochemical measurement results illustrate that a ZnO and SnO/SnO₂ mixed film on alloy anode surface decreases self-corrosion and improves anodic efficiency during discharging. The excessive intermetallic phases lead to the failure of passivation films, acting as micro-cathodes to accelerate self-corrosion.

© 2021 Chongqing University. Publishing services provided by Elsevier B.V. on behalf of KeAi Communications Co. Ltd.

This is an open access article under the CC BY-NC-ND license (<http://creativecommons.org/licenses/by-nc-nd/4.0/>)

Peer review under responsibility of Chongqing University

Keywords: Magnesium alloys; Alloy anode; Self-corrosion; Magnesium-air battery; Discharge performance.

1. Introduction

Metal-air batteries contain a metal anode, an air cathode and electrolyte, have been regarded as promising electricity storage systems for future energy storage because of their low cost and high specific density [1]. Additionally, the cathode (O₂) comes from the air, which reduces the total weight of the battery [2,3]. The Mg-air battery is a type of metal-air battery, which is being considered as next-generation energy storage technology for future energy demand.

Mg anodes have the advantages of a very negative potential (-2.37 V vs. standard hydrogen electrode, SHE), a high Faradic capacity (2.2 Ah g⁻¹), and a low density (1.74 g cm⁻³) [4,5]. Mg-air batteries have a high theoretical voltage (3.09 V) and energy density (6.8 kWh kg⁻¹) [6]. Al-

though the Mg-air battery is a primary battery, the consumed Mg anode can be replaced by a fresh Mg anode to make Mg-air battery "refuelable" [7,8]. However, the metal anode of Mg-air batteries suffers from low anodic efficiency due to its high self-corrosion rate, and the discharge products tend to accumulate on the electrode, suppressing the electrochemical reaction kinetics between Mg anode and aqueous electrolyte. Much effort has been attempted to reduce the corrosion rate by changing the composition of Mg alloy anode [9-11], and by adding corrosion inhibitors in the electrolyte [7,12-15].

Introduction of alloying elements into Mg is one of the most efficient methods to improve its battery performance. Alloying elements including Al, Zn, Pb, Sn, In, Li, Ca and RE (rare earth elements) influence the microstructure and chemical properties of Mg alloy, which could modify the kinetics of anodic or cathodic [16]. Both Zn and Sn are eco-friendly elements with high solid solubility in Mg, 6.2 and 14.5 wt.%, respectively. A small amount of Zn (< 5 wt.%) can refine the

* Corresponding author.

E-mail address: s.wei@auckland.ac.nz (S. Wei).

grain size, while high Zn concentration in Mg forms Mg_xZn_y phases distributed as a network structure along the dendrite and grain boundaries [17]. The Mg_xZn_y phases provide an age-hardening response [18], but large Mg_xZn_y phases can act as the cathode to the Mg matrix and increase the corrosion rate [19,20].

Previous studies have shown that a small amount of Zn can improve the corrosion resistance of Mg alloy and form a protective film [21,22]. During battery discharging, Zn can reduce the pH value of the electrolyte close to the surface, and accelerate the dissolution of discharge products $Mg(OH)_2$ [23]. In our previous research, the environmental-friendly and low-cost Mg-Zn binary alloys have been studied as anode materials for a Mg-air battery [24]. Mg-2Zn alloy anode shows a high utilization efficiency and specific capacity of 54.42% and 1185.50 mAh g^{-1} at 10 mA cm^{-2} , respectively [24]. Mg-Zn based ternary alloys have also shown interesting anodic performance, for example, Chen et al. [25] reported that Mg-6Zn-1Y (ZW61) has a high discharge capacity of 1162.8 mAh g^{-1} and anodic efficiency of 55.1% at the current density of 40 mA cm^{-2} .

Sn has been used as a high-performance anode material for Mg-ion rechargeable batteries due to its high theoretical specific capacity (903 mAh g^{-1}) and low standard H_2 potential (-0.1375 V) [26,27]. We recently reviewed the performance of Mg alloys as anodes for Mg-air batteries with aqueous electrolyte system [16]. The secondary phase Mg_2Sn accelerates the dissolution of Mg anode and breaks the passive film, significantly improving the discharge performance of the Mg-air battery [28]. Gu et al. reported that Mg-4Sn-1Zn-1Ag (TZQ411) had good anodic efficiency of 69.53% at 120 mA cm^{-2} [11]. Although these studies reported that addition of Sn improves the discharge performance of Mg alloy anodes in the Mg-air battery [16,28], the electrochemical behavior and battery properties of ternary Mg-Zn-Sn alloys have not been systematically studied. In this work, the microstructure, electrochemical properties, and battery discharge performance of four ZT alloys have been studied as the anode materials for Mg-air aqueous batteries. The effect of Mg_xZn_y and Mg_2Sn secondary phases on Mg-air battery performance are discussed.

2. Experimental

2.1. Materials

Four Mg-xZn-ySn alloys ($x = 2, 4$ and $y = 1, 3$ wt.%) were prepared in a vacuum induction furnace. High purity raw Mg, Zn and Sn (> 99.9%) materials were melted in a mild steel crucible under argon atmosphere at 720 °C. The melt was stirred well and homogenized before pouring into a steel mould, preheated to 250 °C. For comparison, Mg-2Zn and Mg-4Zn alloys were also prepared via the same casting procedures. The nominal and analyzed compositions of as-cast Mg-Zn and Mg-Zn-Sn (ZT) alloys are presented in Table 1, showing that the alloys have very low concentrations of other elements, Fe, Ni and Cu.

2.2. Microstructure characterization

The microstructure of ZT alloys were examined using optical microscopy (OM, Nikon Eclipse LV100ND), scanning electron microscopy (SEM, Hitachi SU70), and energy dispersive X-ray spectroscopy (EDS, Thermo Scientific Noran System 7). Metallographic specimens of as-cast ZT alloys were ground on SiC papers of grit sizes up to 1200# and cleaned with distilled water. In the final polishing stage, all specimens were carefully polished by 0.05 μm silica in ethanol to obtain high-quality surfaces for microstructure observation. The samples were etched with a solution consisting of 5 mL acetic acid, 6 g picric acid, 10 mL H_2O , and 100 mL ethanol.

2.3. Electrochemical measurements

All Mg alloy samples were ground with abrasive papers up to 1200 grit before electrochemical measurements and battery testing. A typical three electrodes system was used for electrochemical analysis by an electrochemical workstation (BioLogic SP300): Pt plate as a counter electrode, saturated calomel electrode (SCE) as a reference electrode and Mg alloy samples as working electrodes in 3.5 wt.% NaCl solution. Potentiodynamic polarization analysis was conducted at a scan rate of 1 mV s^{-1} after 10 min immersion in the electrolyte. The open-circuit potential (OCP) was recorded in a 3.5 wt.% NaCl solution for 30 min waiting time to achieve a stable surface. Electrochemical impedance spectroscopy (EIS) was conducted at OCP with frequencies of 100 kHz to 0.05 Hz and 5 mV voltage amplitude. The potentiodynamic polarization and EIS tests were performed more than two times to ensure the repeatability of the data. In addition, Atomic Force Microscope (MFP-3D Origin AFM) combined with Scanning Kelvin Probe force microscopy (SKPFM) was used to study the volta potential difference between intermetallic compounds and Mg matrix. The silicon probe is coated with a Cr/Pt conductive coating (Budget Sensors Electritap300-G, resonant frequency 300 kHz).

2.4. Battery discharge and performance calculation

The battery discharge properties were tested by a LAND battery test system (CT3001A) in a Mg-air battery test kit at four current densities of 1, 2, 5, and 10 mA cm^{-2} as shown in Fig. 1. Mg alloys worked as anodes with an exposed area of approximately 1.77 cm^2 (1.5 cm diameter) in a 3.5 wt.% NaCl solution electrolyte. The cathode was a commercial air cathode with 0.3 mg cm^{-2} 40% platinum nanoparticles as catalysts (Fuel Cell Store. Ltd). After battery discharge testing, the reaction products on the anode surface were removed by a 200 g L^{-1} chromic acid solution. Then, the surface morphologies were characterized by SEM (SE, 10 kV). The specific capacity, anodic efficiency and specific energy density were calculated as follows [6,24,29]:

$$\text{Utilization Efficiency (\%)} = \frac{W_{\text{theo}}}{\Delta W} \times 100\%$$

Table 1
Chemical compositions of Mg-Zn and ZT alloys (analyzed by Agilent 7700 ICP-MS).

Nominal composition wt.%	Analyzed composition wt.%							
	Zn	Sn	Al	Si	Mn	Fe	Ni	Cu
Mg-2Zn	2.376	-	0.013	0.077	0.013	0.006	0.004	0.001
Mg-2Zn-1Sn (ZT21)	2.254	1.096	0.014	0.041	0.013	0.012	0.000	0.003
Mg-2Zn-3Sn (ZT23)	2.169	3.143	0.007	0.038	0.013	0.087	0.000	0.003
Mg-4Zn	4.137	-	0.009	0.0527	0.0115	-	0.001	0.001
Mg-4Zn-1Sn (ZT41)	4.157	1.094	0.008	0.042	0.015	0.015	0.000	0.002
Mg-4Zn-3Sn (ZT43)	3.847	2.997	0.007	0.040	0.014	0.011	0.000	0.002

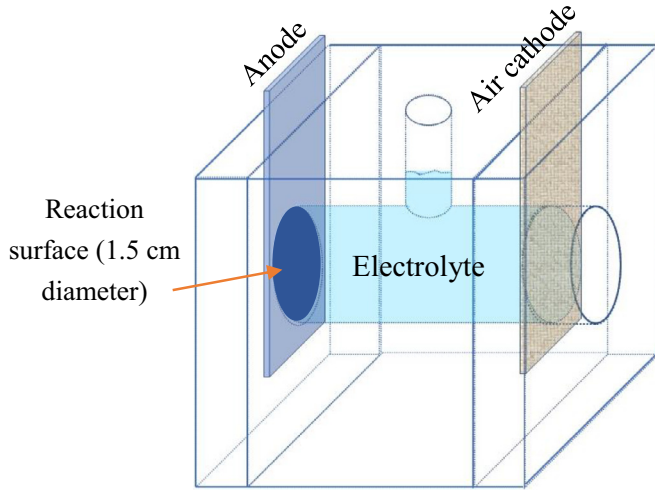


Fig. 1. Schematic of the Mg-air cell for battery discharge test.

$$W_{\text{theo}} = \frac{I \times t}{F \times \sum \left(\frac{x_i \times n_i}{m_i} \right)}$$

$$\text{Specific capacity (mAh} \cdot \text{g}^{-1}) = \frac{I \times t}{\Delta W} \times 1000$$

$$\text{Specific energy density (mWh} \cdot \text{g}^{-1}) = \frac{U \times I \times t}{\Delta W} \times 1000$$

Where ΔW (g) is the weight loss of samples during the discharge, W_{theo} (g) is the theoretical weight loss, U is the cell voltage, I is the discharge current (A), t is discharge time (h), F is the Faraday constant (26.8 Ah mol⁻¹), and x_i , n_i , m_i represent the mass fraction, number of exchanged electrons and atomic weight, respectively.

3. Results and discussion

3.1. Microstructure analysis

The optical micrographs of as-cast ZT21, ZT23, ZT41 and ZT43 alloys are shown in Fig. 2 (a–d). These as-cast ZT alloys exhibit a typical dendritic microstructure, which consists of α -Mg dendrites and intermetallic phases at dendritic regions and grain boundaries. Backscattered electron SEM (BSE-SEM) technique has been used for characterising these four alloys, and results are shown in Fig. 2 (e–h).

Table 2

Electrochemical parameters of Mg-Zn and ZT alloys obtained from polarization curves.

Alloys	E_{corr} (vs. SCE)/ V	j_{corr} / $\mu\text{A} \cdot \text{cm}^{-2}$	Refs.
Mg-2Zn	-1.662	33.77	[24]
ZT21	-1.678 \pm 0.005	30.21 \pm 1.02	This work
ZT23	-1.698 \pm 0.007	45.54 \pm 2.28	This work
Mg-4Zn	-1.655	21.05	[24]
ZT41	-1.685 \pm 0.005	27.34 \pm 0.75	This work
ZT43	-1.683 \pm 0.009	24.67 \pm 3.84	This work

With increasing Zn and Sn content, the contrast between α -Mg dendrites and interdendritic regions increases, indicating that solute elements Zn and Sn segregate around the interdendritic regions and grain boundaries. The intermetallic phases in ZT alloys are distributed along dendritic regions and grain boundaries.

Wei et al. [30] have conducted a comprehensive microstructure analysis on Mg-Zn-Sn alloys and reported that the microstructure of as-cast ZT43 alloy consists of α -Mg, Mg₂Sn phase, eutectic phase (α -Mg+Mg₄Zn₇), and globular-shaped phase ((α -Mg +Mg₄Zn₇)+Mg₂Sn). High magnification SEM images and EDS results in Fig. 2(i, j) confirm that ZT alloys have three types of intermetallic phases: eutectic phase A (α -Mg+Mg₄Zn₇), Mg₂Sn phase B and a combination of two structures particle C. Instead of globular-shape, particle C displays as dolphin-like morphology with a hybrid structure of eutectic phase (α -Mg+Mg₄Zn₇) on the right side and Mg₂Sn on the left side. Thus, the microstructure of as-cast ZT alloys consists of α -Mg, Mg₂Sn phase, eutectic phase (α -Mg+Mg₄Zn₇), and the hybrid phase ((α -Mg +Mg₄Zn₇)+Mg₂Sn).

3.2. Electrochemical analysis

In Mg-air aqueous batteries, a high self-corrosion rate is a critical problem for Mg metal anodes. The corrosion performances of ZT alloys were evaluated by potentiodynamic polarization and electrochemical impedance spectroscopy (EIS). For comparison purpose, the potentiodynamic polarization and EIS results of Mg-2Zn and Mg-4Zn were also presented. Fig. 3 shows the Tafel curves of Mg-Zn and ZT alloys, and the fitting value of E_{corr} and j_{corr} are presented in Table 2. The corrosion potential E_{corr} of Mg-Zn alloys shows a decrease trend by adding Sn alloy element, indicating that Sn

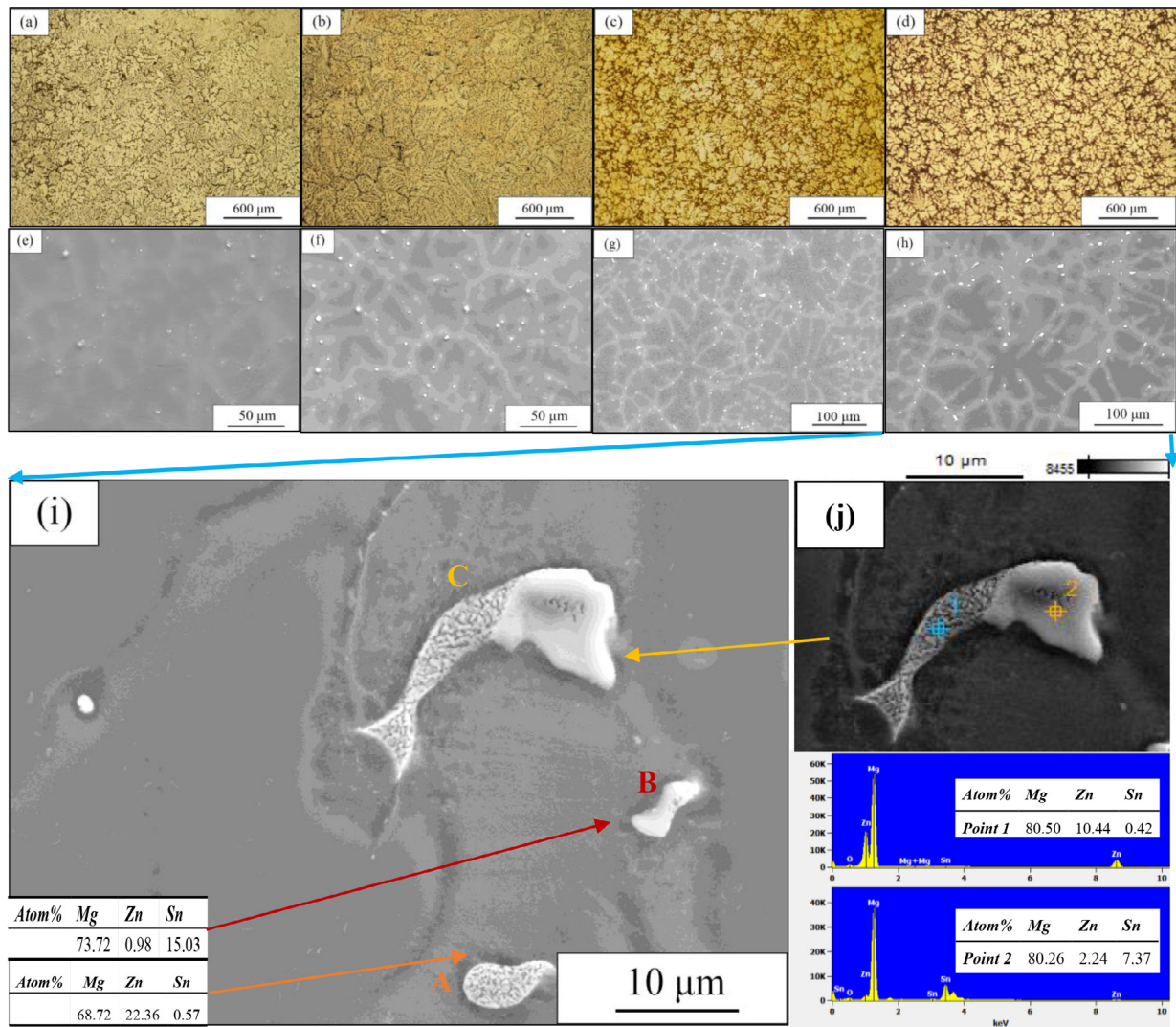


Fig. 2. The microstructure of as-cast Mg-Zn-Sn (ZT) alloys: (a) and (e) ZT21, (b) and (f) ZT23, (c) and (g) ZT41 and (d) and (h) ZT43. (i) and (j) shows SEM-EDS elemental analysis of the intermetallic phases in ZT43 alloy.

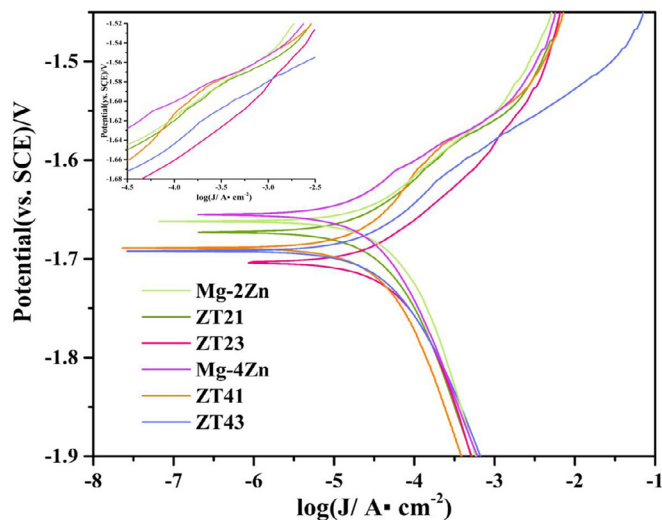


Fig. 3. Potentiodynamic polarization curves of Mg-Zn and ZT alloys in 3.5 wt.% NaCl electrolyte solution.

can reduce the cathodic kinetics. The cathode polarization curve indicates the hydrogen evolution rate, showing that ZT alloys have a low hydrogen evolution rate than Mg-Zn alloys. In other words, addition of Sn improves corrosion resistance of Mg-Zn alloys.

However, corrosion current density j_{corr} of Mg-Zn alloys varied with the amount of Sn content. It is known that Mg has a “negative difference effect” in which the rate of partial cathodic reaction increases with applied anodic potential. Addition of Sn and Zn has affected the anodic reaction of Mg alloys in NaCl solution. At the anode part of the Tafel curve, ZT21 and ZT41 alloys show apparent passive points (insert image in Fig. 3), indicating that Mg-xZn-1Sn alloys can produce passive films on the surface of the metal anode to decrease their corrosion progress. This agrees with the report by Jiang et al. [31] that solute Sn in Mg matrix may form SnO_2 at alloy surface in an aqueous solution, improving alloy’s corrosion resistance. However, when the concentration of Sn is higher than 2 wt.%,

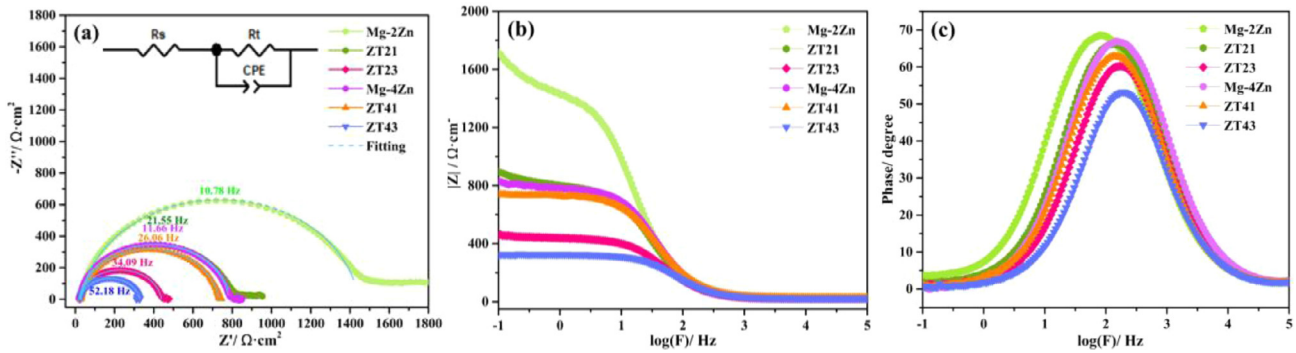


Fig. 4. Electrochemical impedance spectra of Mg-Zn and ZT alloys in 3.5 wt.% NaCl solution: (a) Nyquist plots, (b) Bode plots of impedance modulus vs. frequency, and (c) Bode plots of phase angle vs. frequency.

Table 3

Fitting the EIS parameters of Mg-Zn and ZT alloys.

Materials	R_s / Ω	R_t / Ω	$CPE-T \times 10^{-5}$	CPE-P
Mg-2Zn	26.80 ± 2.01	1561.50 ± 146.50	1.324 ± 0.151	0.936 ± 0.0071
ZT21	21.19 ± 1.27	649.95 ± 119.45	1.543 ± 0.152	0.933 ± 0.0032
ZT23	22.75 ± 1.94	632.45 ± 214.95	1.490 ± 0.011	0.931 ± 0.0011
Mg-4Zn	24.76 ± 3.88	1153.15 ± 389.85	1.164 ± 0.043	0.940 ± 0.000
ZT41	24.10 ± 3.99	792.85 ± 89.05	1.282 ± 0.031	0.937 ± 0.001
ZT43	24.52 ± 1.05	287.55 ± 14.65	1.581 ± 0.114	0.924 ± 0.005

a large amount of Mg_2Sn increases corrosion by galvanic effect [31].

The EIS of Mg-Zn and ZT alloys were investigated at open circuit potential (OCP). The Nyquist plot and their fitting circuit are shown in Fig.4(a), in which R_s is the solution resistance, R_t is the charge transfer resistance that equals to the diameters of capacitive semi-circles, and CPE represents the electric double-layer capacitance at the interface between the anode surface and the NaCl solution. In general, relatively high CPE values indicate large active corrosion areas and low R_t values, representing poor corrosion performance [4,32].

It can be seen from Table 3 that ZT alloys have larger CPE values than Mg-Zn alloys, implying that a larger active area for the discharge reaction. ZT alloys also show much lower R_t than that of Mg-Zn binary alloys, which means that ZT alloys have lower charge transfer resistance than those of Mg-Zn alloys. Thus, the protection of initial oxide films of ZT alloys is not better than Mg-Zn alloys. Fig. 4(b) shows the Bode plot in terms of the $|Z|$ vs frequency. For all materials tested, the impedance increases with decreasing frequency and then maintains a stable value at low frequency. The impedance modulus is generally employed to evaluate the corrosion resistance [33,34]. Materials with higher impedance modulus usually mean higher corrosion resistance. In this work, the impedance modulus was found to decrease in the order of Mg-2 Zn > ZT21 > Mg-4 Zn > ZT41 > ZT23 > ZT43.

Volta potential differences of metal microstructure have been used to predict corrosion behavior [35,36]. This method can measure the potential in a small area to investigate localized corrosion and micro-galvanic activities [37]. In this research, we have conducted volta potential measurements on secondary phases of ZT43 alloy, Mg-4Zn and Mg-3Sn alloys

for comparison, as shown in Fig. 5. The results indicate that all the intermetallic compounds (bright particles) have higher Volta potential than the surrounding Mg matrix. The volta potentials of Mg_2Sn and Mg_4Zn_7 phases are around 120 and 55 mV, respectively. Therefore, Mg_2Sn phase acts as stronger cathodic sites than Mg_4Zn_7 for corrosion, thus increases the electrochemical activity of Mg-Zn alloy, constant with the results from Tafel curves and EIS.

3.3. Discharge behavior

The battery discharge performances of ZT alloy anodes were studied in Mg-air electrochemical cells, and the results are shown in Fig. 6. Discharge properties of Mg-2Zn and Mg-4Zn alloys are presented for comparison [24]. ZT alloys display improved discharge behaviors. Fig. 6 shows that the operating voltages of ZT alloy anodes are higher than Mg-Zn alloy. Fig. 6(e) shows an interesting phenomenon, jagged fluctuations, observed in the discharge curves, which represents the release of hydrogen as a side reaction. Compared to Mg-Zn alloys, ZT alloys have minor fluctuations, especially ZT21 alloy shows a very smooth discharge reaction at low current densities.

At 1 and 2 $mA\ cm^{-2}$, all Mg alloy anodes can be discharged up to 20 h. When the current density increases to 5 and 10 $mA\ cm^{-2}$, the discharge voltage fluctuate severely. However, ZT21 and ZT23 anodes can still discharge smoothly for 20 h. The deteriorated battery performance of anode is directly related to the broken balance between the reaction products deposition and detachment [4]. Intermetallic compounds Mg_2Sn or solid soluble Sn may cause easy detachment or dissolution of discharge products. Compared to ZT21 and ZT23

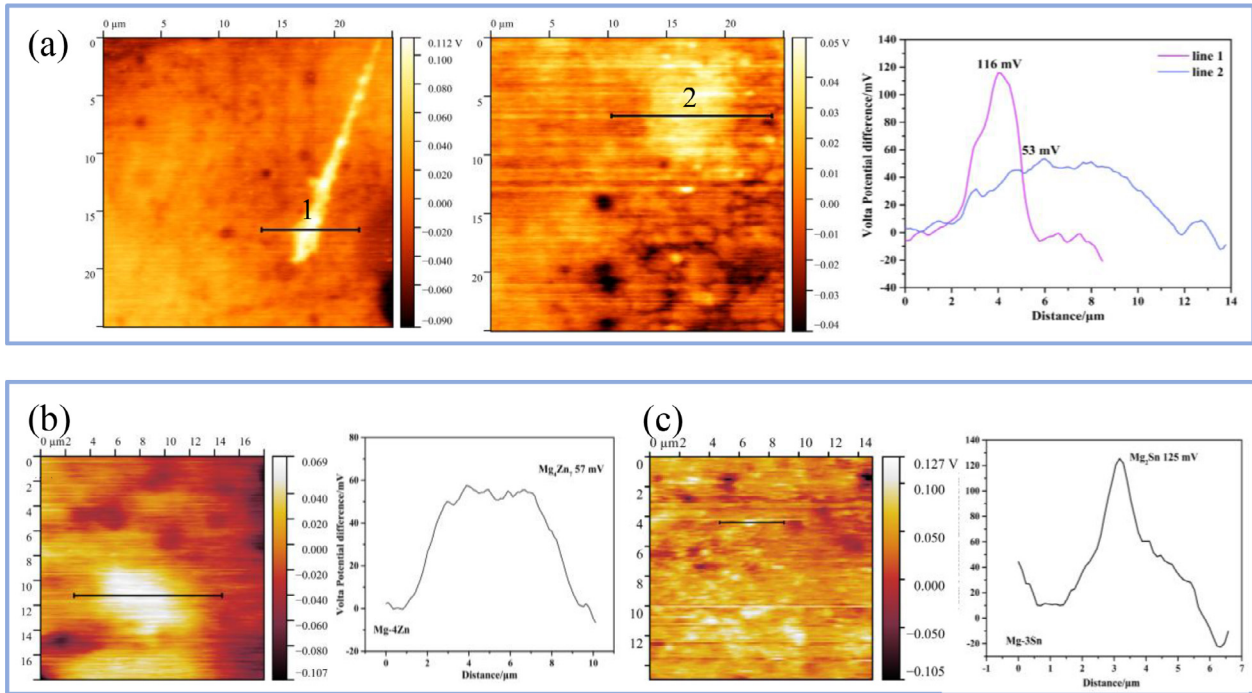


Fig. 5. Volta potential map and potential curves of: (a) Mg-4Zn-3Sn (ZT43), (b) Mg-4 Zn and (c) Mg-3Sn alloys by SKPFM.

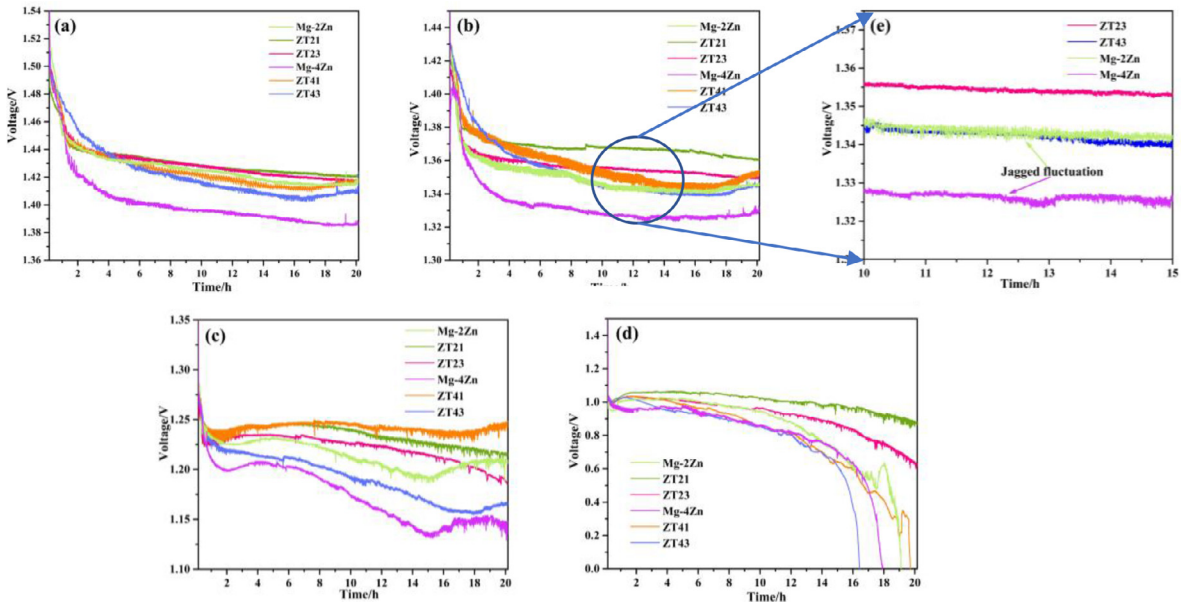


Fig. 6. Discharge curves of Mg-Zn and ZT alloy anodes at four current densities: (a) 1 mA cm^{-2} ; (b) and (e) 2 mA cm^{-2} ; (c) 5 mA cm^{-2} , and (d) 10 mA cm^{-2} in 3.5 wt.% NaCl solution. The cathode is a Pt catalyst carbon cloth [24].

alloys, the turbulent voltages of ZT41 and ZT43 are caused by the larger number of intermetallic compounds than that in ZT21 and ZT23. In addition, Zn and Sn segregated on interdendritic regions and grain boundaries in Mg alloys could accelerate the self-corrosion, and affect the accumulation of reaction products on the anode surface [24].

The battery properties of ZT alloys anodes in Mg-air batteries are shown in Fig. 7(a, b). The battery discharge performance of recast Mg, Mg-Zn alloy are included for com-

parison [24]. ZT alloys have much higher discharge voltage, anodic efficiency, specific capacity, and specific energy density than Mg-Zn and pure Mg at the current density of 1 to 5 mA cm^{-2} . ZT23 alloy shows the highest utilization efficiency of 47.2%, specific capacity of 1009 mAh g^{-1} and specific energy density of 1367 mWh g^{-1} at 2 mA cm^{-2} . ZT21 and Mg-2Zn alloy anodes show the similar anodic efficiency and specific capacity, which are higher than other anode materials at 10 mA cm^{-2} . Although the properties of

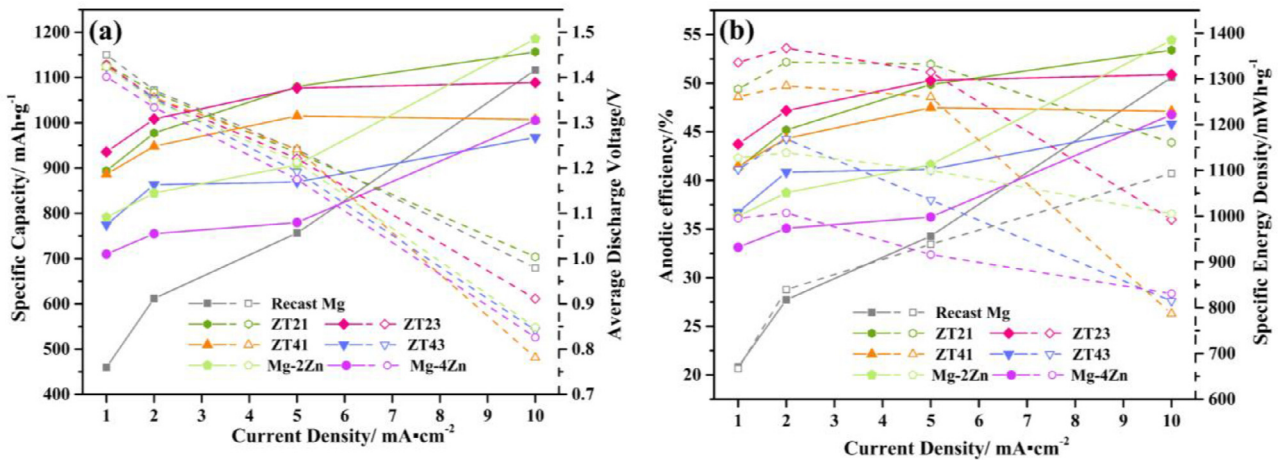


Fig. 7. Discharge properties of Mg-Zn and ZT alloy anodes at different current densities for 20 h: (a) average discharge voltage and specific capacity vs current density, (b) anodic efficiency and specific energy density vs current density [24].

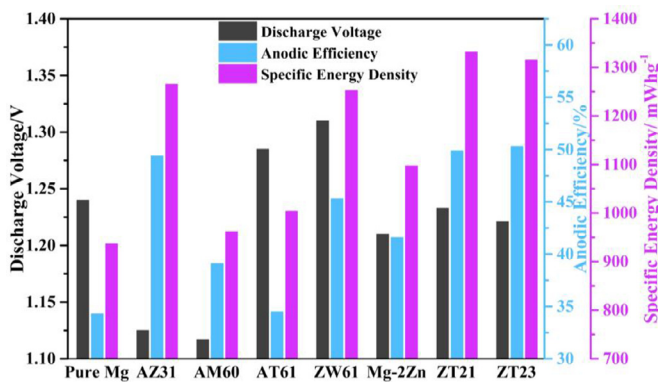


Fig. 8. Battery discharge performance of ZT anodes comparing with pure Mg and commercial alloys anodes at the current density 5 mA cm⁻² [16,24,25,38–40].

ZT41 and ZT43 alloys are not better than those of ZT21 and ZT23 alloys, they still much better than Mg-4Zn at the current densities of 1, 2, 5 mA cm⁻². With increasing current density from 1 to 10 mA cm⁻², the anodic efficiencies of pure Mg changes from 20.84 to 50.60%, while the anodic efficiencies of ZT21 alloy anode increases from 41.28 to 53.41%. Compared to recast Mg and Mg-Zn alloys, ZT alloy anodes demonstrate a much stable discharge performance. This may be related to the formation, accumulation and detachment of discharge product on the anode surface.

Gu et al. have studied the discharge performance of Mg-Sn-Zn-Ag alloy anode with three different Sn concentrations (2, 4 and 8 wt.%), and reported that Mg-4Sn-1Zn-1Ag (TZQ411) has high anodic efficiency of 69.53% at 120 mA cm⁻² and 45.30% at 10 mA cm⁻² [11]. Compared to TZQ411, ZT21 and ZT23 show better anodic efficiency at 53.41% and 50.90% at 10 mA cm⁻², respectively. Fig. 8 compares the battery performance of ZT21 and ZT23 anodes with commercial Mg anodes such as AZ31 and AM60 at 5 mA cm⁻² [16,24,25,38–40]. The specific energy density

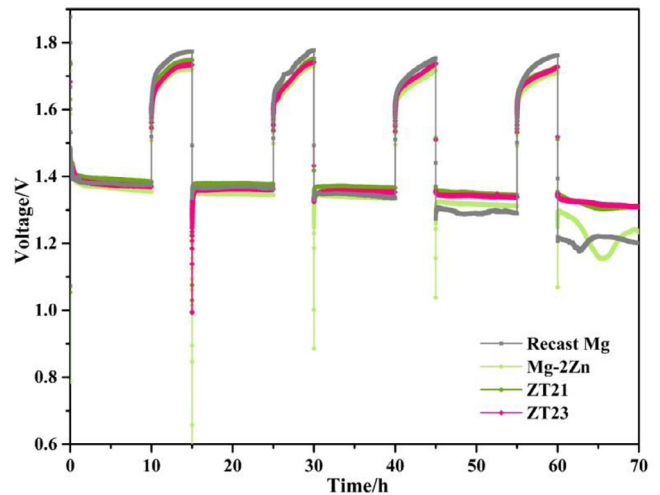


Fig. 9. Intermittent discharge of Mg-air battery with recast Mg, Mg-Zn and ZT anodes at 2 mA cm⁻² in 3.5 wt.% NaCl solution.

and anodic efficiency of ZT alloy are much better than pure Mg, AZ31 and AM60 alloys.

Since the discharge in practical application runs periodically, the intermittent discharge is a useful test to simulate the practical application. ZT21 and ZT23 alloys have good discharge performance during 20 h time, so they are tested for intermittent discharging. Intermittent discharge testing was also performed on recast Mg and Mg-2Zn alloy anodes for comparison purpose, which was carried out for 10 h at a constant current density 2 mA cm⁻² and stop for 5 h as one cycle. The test is terminated at the fifth cycle as these anodes showed a significant voltage drop. Fig. 9 shows that ZT, Mg-2Zn and recast Mg anodes exhibited very similar behavior in the first 4 cycles with discharge voltages of ~1.4 V. When the discharge stopped, the OCV increased to 1.8 V. However, at the following cycles, the voltage drop of pure Mg and Mg-Zn were more apparent than ZT alloys. The percentage of voltage drop are calculated after 30 min discharge for each

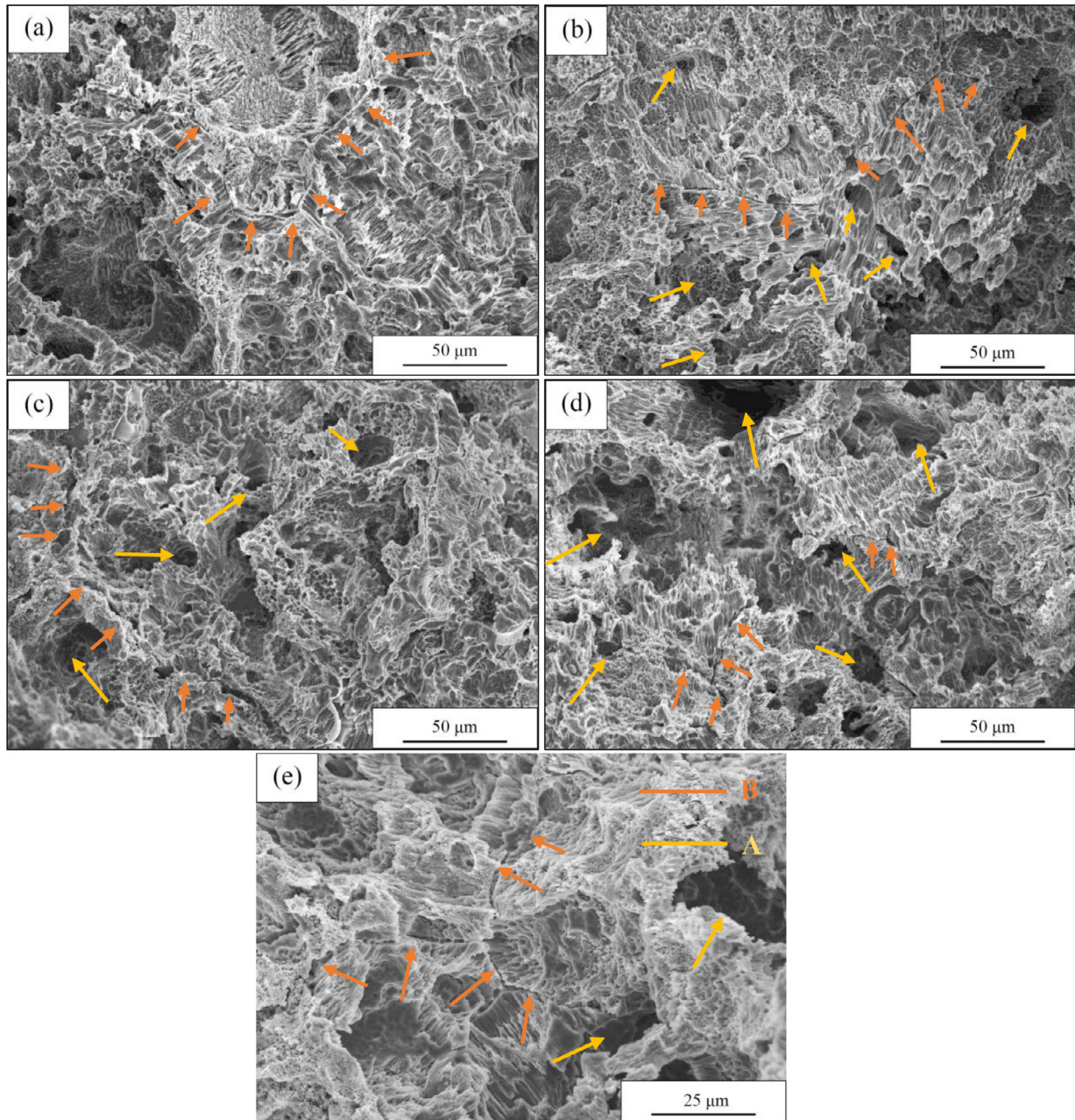


Fig. 10. Surface morphologies of anodes after discharge: (a) ZT21, (b) ZT23, (c) ZT41, (d) and (e) ZT43 at 2 mA cm^{-2} for 20 h in 3.5 wt.% NaCl solution.

Table 4
The voltage drop of 5 cycles (%), compared with the previous cycle.

Voltage Drop/%	2nd	3th	4th	5th	Total
Recast Mg	0.83	1.61	3.80	6.66	12.39
Mg-2Zn	1.40	0.63	1.57	7.34	10.64
ZT21	1.04	0.65	1.40	2.69	5.67
ZT23	1.12	0.53	0.98	1.72	4.28

cycle, and results are listed in Table 4, indicating that ZT21 and ZT23 have more stable discharge voltage than Mg and Mg-Zn.

At the fifth discharge cycle, the voltages of ZT21 and ZT23 are around 1.3 V, while the Mg and Mg-2Zn's voltages were

around 1.2 V. The voltage drops percentages of Mg, Mg-2Zn, ZT21 and ZT23 are 12.39%, 10.64%, 5.67%, and 4.28%, respectively. As the discharge products accumulated on the anode and electrolyte interface, which cause a decrease of operating voltage. This result indicates that Sn could minimize the discharge product accumulation, improving the discharge stability.

3.4. Anode surface analysis after battery discharging

Fig. 10 shows the surface morphology of ZT anode after discharge for 20 h at 2 mA cm^{-2} . ZT anodes have relatively fine corrosion holes uniformly distributed inside grains

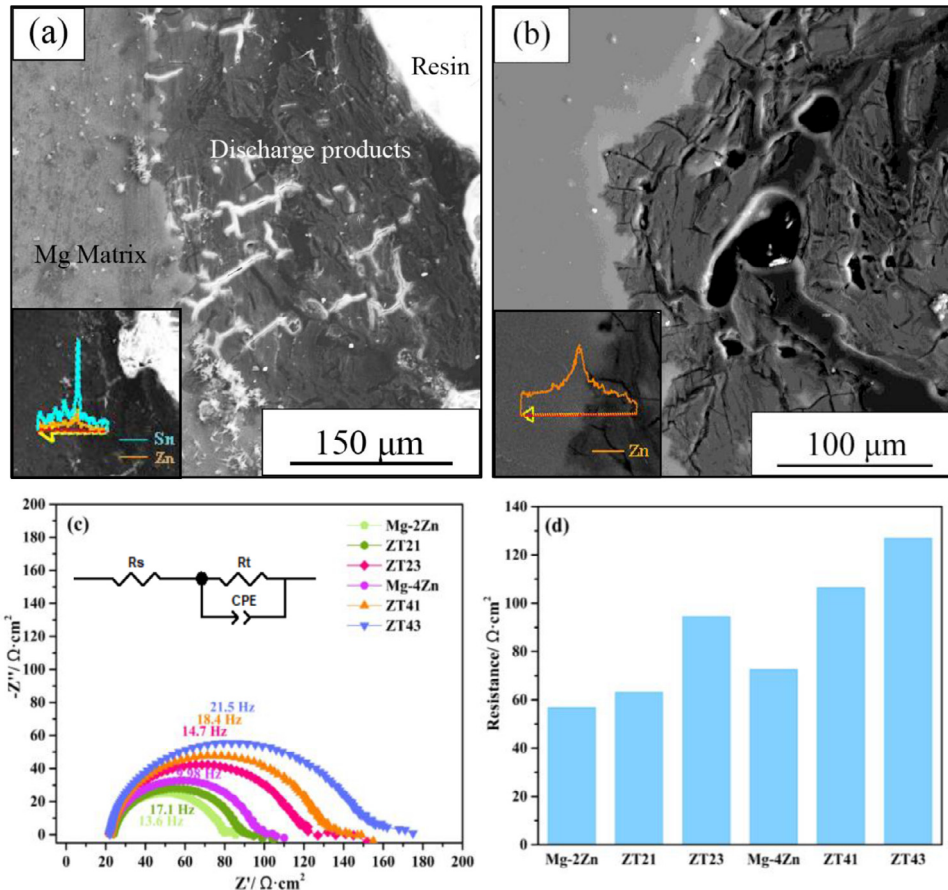


Fig. 11. Cross-section of (a) ZT21 and (b) Mg-2 Zn alloy anodes discharge at 2 mA cm^{-2} for 20 h with discharge products and their EDS line scan, (c) EIS and the fitting circuit of the investigated alloy anodes after discharge at 2 mA cm^{-2} for 30 min, and (d) Charge transfer resistance of the EIS results.

(pointed by arrow A), and obvious microcracks extend along the grain boundaries (pointed by arrow B). The surface of ZT21 and ZT23 looks relatively flat, while ZT41 and ZT43 have obviously deep and large corrosion pits. Since the standard potential of Sn (-0.1375 V) and Zn (-0.7618 V) are much positive than that of Mg (-2.372 V) [27], the Zn and Sn-rich site near the dendritic and grain boundaries may act as a cathode to accelerate micro-galvanic corrosion of the surrounding matrix. The cracks at the grain boundaries shown in Fig 10(e) may come from the Zn and Sn-rich regions. According to the SKPFM result in Section 3.2, the intermetallics are more positive than the Mg matrix. The corrosion pits in area A came from the intermetallic compounds and distributed evenly inside the grains, which accelerate the corrosion of Mg matrix and the discharge performance. However, the deep pits make the corrosion products not easy to fall off.

Fig. 11(a) and (b) show the cross-section of Mg-2Zn and ZT21 anodes after discharge for 20 h at 2 mA cm^{-2} . EDS line scan in Fig.11(a) shows that the discharge reaction interface of Mg-2 Zn and ZT21 alloy are enriched with Zn and Zn/Sn elements, respectively, implying that the anode surfaces are protected by ZnO and ZnO/SnO_x ($x = 1$ or 2), consistent with the corrosion in NaCl solution [41–43]. The EIS test at OCV after discharge at 2 mA cm^{-2} for 30 min is shown in Fig.11(c)

and (d). The charge transfer resistances (R_t) is related to the corrosion products film. The R_t of Mg-2Zn-ySn are lower than those of Mg-4Zn-ySn ($y = 0, 1$ and 3), so the alloys with high Zn content exist thick discharge product layers. This result is consistent with the previous result that Mg alloys with high Zn content have a large amount of intermetallic compounds to facilitate self-corrosion and discharge products accumulation [24].

The R_t of Mg alloys follows the order of $\text{Mg-xZn} < \text{Mg-xZn-1Sn} < \text{Mg-xZn-3Sn}$ ($x = 2, 4$), different from the EIS in Section 3.2 due to the different sample conditions explained below. The samples before discharge have thin oxide films, while after 30 min discharge, a layer of discharge products form and attach on the anode surface. The high R_t of ZT alloys may come from Sn containing outer layer film of stable SnO/SnO₂ and the severe deep pitting of ZT alloys (Fig.10), leading to the difficult falling-off of the discharge products on the anode surface and further decrease self-corrosion. Thus, the mixed film of ZnO and SnO/SnO₂ has a better protective effect on Mg alloy than ZnO film as Sn decreases the self-corrosion and protects Mg alloy, improving anodic efficiency during discharge. Therefore, the ZT anode exhibits outstanding battery performance that has a good application potential as anode material for Mg-air battery.

4. Conclusion

The effect of Sn on the microstructure, electrochemical and discharge properties of Mg-Zn alloy anodes for Mg-air battery have been investigated. The addition of Sn affects the microstructure of Mg-Zn alloys, forming SnO or SnO₂ film on the anodes during discharge and significantly improves the battery performance of Mg-Zn alloy at low current densities (< 10 mA cm⁻²). Sn can also stimulate the electrochemical activity of Mg matrix during discharge. Mg₂Sn phase has stronger cathodic effect than Mg_xZn_y phase. Mg air battery with Mg-Zn-Sn alloy anode has significantly higher operating voltage than Mg-Zn anode. Compared to Mg-2Zn, the anodic efficiency of ZT23 increase from 41.6% to 50.3% at 5 mA cm⁻². Among the ZT anodes, ZT23 has the best battery performance at low current density (< 5 mA cm⁻²) and shows the high energy density of 1367 mWh g⁻¹ at 2 mA cm⁻².

Acknowledgments

This work is partially supported by the Marsden Fund managed by the Royal Society of New Zealand Te Apārangi (Fast-Start Marsden Grant project No. UOA1817). Fanglei Tong is thankful for the scholarship from China Scholarship Council (No.201808060410).

References

- [1] J. Lee, S.T. Kim, R. Cao, N. Choi, M. Liu, K.T. Lee, J. Cho, *Adv. Energy Mater.* 1 (1) (2011) 34–50, doi:10.1002/aenm.201000010.
- [2] F. Cheng, J. Chen, *Chem. Soc. Rev.* 41 (6) (2012) 2172–2192 Mar 21, doi:10.1039/c1cs15228a.
- [3] M. Deng, L. Wang, D. Höche, S.V. Lamaka, P. Jiang, D. Snihirova, N. Scharnagl, M.L. Zheludkevich, *J. Power Sources* 472 (2020), doi:10.1016/j.jpowsour.2020.228528.
- [4] X. Liu, J. Xue, D. Zhang, *J. Alloy. Compd.* 790 (2019) 822–828, doi:10.1016/j.jallcom.2019.03.260.
- [5] L. Shen, G. Zhang, T. Venter, M. Biesalski, B.J.M. Etzold, *Electrochim. Acta* 298 (2019) 389–399, doi:10.1016/j.electacta.2018.12.077.
- [6] M. Deng, D. Höche, S.V. Lamaka, D. Snihirova, M.L. Zheludkevich, *J. Power Sources* 396 (2018) 109–118, doi:10.1016/j.jpowsour.2018.05.090.
- [7] T. Zhang, Z. Tao, J. Chen, *Mater. Horiz.* 1 (2) (2014) 196–206, doi:10.1039/c3mh00059a.
- [8] H. Yang, L. Wu, B. Jiang, B. Lei, W. Liu, J. Song, A. Atrens, G. Huang, D. Zhang, *F. Pan, J. Electrochem. Soc.* 167 (11) (2020), doi:10.1149/1945-7111/aba339.
- [9] S. Yuan, H. Lu, Z. Sun, L. Fan, X. Zhu, W. Zhang, *J. Electrochem. Soc.* 163 (7) (2016) A1181–A1187, doi:10.1149/2.0371607jes.
- [10] X. Liu, J. Xue, S. Liu, *Mater. Des.* 160 (2018) 138–146, doi:10.1016/j.matdes.2018.09.011.
- [11] X. Gu, W. Cheng, S. Cheng, H. Yu, Z. Wang, H. Wang, L. Wang, *J. Electrochem. Soc.* 167 (2) (2020), doi:10.1149/1945-7111/ab6284.
- [12] M.A. Deyab, *J. Power Sources* 325 (2016) 98–103, doi:10.1016/j.jpowsour.2016.06.006.
- [13] L. Wang, D. Snihirova, M. Deng, B. Vaghefinazari, S.V. Lamaka, D. Höche, M.L. Zheludkevich, *J. Power Sources* 460 (2020), doi:10.1016/j.jpowsour.2020.228106.
- [14] J. Zhang, J. Ma, G. Wang, Y. Li, A.A. Volinsky, *J. Electrochem. Soc.* 166 (6) (2019) A1103–A1106, doi:10.1149/2.0821906jes.
- [15] J. Du, Z. Wang, Y. Niu, W. Duan, Z. Wu, *J. Power Sources* 247 (2014) 840–844, doi:10.1016/j.jpowsour.2013.09.025.
- [16] F. Tong, S. Wei, X. Chen, W. Gao, *J. Magnes. Alloy.* (2021), doi:10.1016/j.jma.2021.04.011.
- [17] S. Cai, T. Lei, N. Li, F. Feng, *Mater. Sci. Eng. C* 32 (8) (2012) 2570–2577, doi:10.1016/j.msec.2012.07.042.
- [18] K. Gusieva, C.H.J. Davies, J.R. Scully, N. Birbilis, *Int. Mater. Rev.* 60 (3) (2014) 169–194, doi:10.1179/1743280414y.0000000046.
- [19] Y. Song, E.H. Han, D. Shan, C.D. Yim, B.S. You, *Corros. Sci.* 60 (2012) 238–245, doi:10.1016/j.corsci.2012.03.030.
- [20] Y. Song, E.H. Han, D. Shan, C.D. Yim, B.S. You, *Corros. Sci.* 65 (2012) 322–330, doi:10.1016/j.corsci.2012.08.037.
- [21] G. Bi, Y. Li, S. Zang, J. Zhang, Y. Ma, Y. Hao, *J. Magnes. Alloy.* 2 (1) (2014) 64–71, doi:10.1016/j.jma.2014.03.002.
- [22] H. Ha, J. Kang, J. Yang, C. Yim, B. You, *Corros. Sci.* 75 (2013) 426–433, doi:10.1016/j.corsci.2013.06.027.
- [23] N. Wang, R. Wang, C. Peng, Y. Feng, *J. Cent. South Univ.* (2012), doi:10.1007/s11771-012-0965-x.
- [24] F. Tong, X. Chen, Q. Wang, S. Wei, W. Gao, *J. Alloy. Compd.* 857 (2021) 157579, doi:10.1016/j.jallcom.2020.157579.
- [25] X. Chen, Q. Zou, Q. Le, J. Hou, R. Guo, H. Wang, C. Hu, L. Bao, T. Wang, D. Zhao, F. Yu, A. Atrens, *J. Power Sources* 451 (2020), doi:10.1016/j.jpowsour.2020.227807.
- [26] M. Song, T. Zhang, J. Niu, H. Gao, Y. Shi, Y. Zhang, W. Ma, Z. Zhang, *J. Power Sources* 451 (2020), doi:10.1016/j.jpowsour.2020.227735.
- [27] P. Vanýsek, *Handbook of Chemistry*, in: Haynes, M. William (Eds.), *Handbook of Chemistry and Physics* (93rd ed.), CRC Press, 2012, pp. 5–80.
- [28] H. Xiong, K. Yu, X. Yin, Y. Dai, Y. Yan, H. Zhu, *J. Alloy. Compd.* 708 (2017) 652–661, doi:10.1016/j.jallcom.2016.12.172.
- [29] F. Movassagh-Alanagh, A. Bordbar-Khiabani, A. Ahangari-Asl, *Int. J. Hydrog. Energy* 44 (49) (2019) 26794–26806, doi:10.1016/j.ijhydene.2019.08.184.
- [30] S. Wei, T. Zhu, M. Hodgson, W. Gao, *Mater. Sci. Eng. A* 585 (2013) 139–148, doi:10.1016/j.msea.2013.07.051.
- [31] W. Jiang, J. Wang, W. Zhao, Q. Liu, D. Jiang, S. Guo, *J. Magnes. Alloy.* 7 (1) (2019) 15–26, doi:10.1016/j.jma.2019.02.002.
- [32] S. Cheng, W. Cheng, X. Gu, H. Yu, Z. Wang, H. Wang, L. Wang, *J. Alloy. Compd.* 823 (2020), doi:10.1016/j.jallcom.2020.153779.
- [33] A. Bordbar-Khiabani, B. Yarmand, M. Mozafari, *Mater Lett* 258 (2020) 126779, doi:10.1016/j.matlet.2019.126779.
- [34] A. Bordbar-Khiabani, S. Ebrahimi, B. Yarmand, *Corros. Sci.* 173 (2020) 108781, doi:10.1016/j.corsci.2020.108781.
- [35] C. Örnek, D.L. Engelberg, *Corros. Sci.* 99 (2015) 164–171, doi:10.1016/j.corsci.2015.06.035.
- [36] M. Rohwerder, F. Turcu, *Electrochim. Acta* 53 (2) (2007) 290–299, doi:10.1016/j.electacta.2007.03.016.
- [37] C. Örnek, C. Leygraf, J. Pan, *Corros. Eng. Sci. Technol.* 54 (3) (2019) 185–198, doi:10.1080/1478422X.2019.1583436.
- [38] Y. Ma, N. Li, D. Li, M. Zhang, X. Huang, *J. Power Sources* 196 (4) (2011) 2346–2350, doi:10.1016/j.jpowsour.2010.07.097.
- [39] M. Yuasa, X. Huang, K. Suzuki, M. Mabuchi, Y. Chino, *J. Power Sources* 297 (2015) 449–456, doi:10.1016/j.jpowsour.2015.08.042.
- [40] H. Xiong, H. Zhu, J. Luo, K. Yu, C. Shi, H. Fang, Y. Zhang, *J. Mater. Eng. Perform.* 26 (6) (2017) 2901–2911, doi:10.1007/s11665-017-2733-4.
- [41] J. Yang, C.D. Yim, B.S. You, *J. Electrochem. Soc.* 163 (14) (2016) C839–C844, doi:10.1149/2.0401614jes.
- [42] M. Esmaily, J.E. Svensson, S. Fajardo, N. Birbilis, G.S. Frankel, S. Virtanen, R. Arrabal, S. Thomas, L.G. Johansson, *Prog. Mater. Sci.* 89 (2017) 92–193, doi:10.1016/j.pmatsci.2017.04.011.
- [43] K.A. Unocic, H.H. Elsentriecy, M.P. Brady, H.M. Meyer, G.L. Song, M. Fayek, R.A. Meisner, B. Davis, *J. Electrochem. Soc.* 161 (6) (2014) C302–C311, doi:10.1149/2.024406jes.